Pure Appl. Chem., ASAP Article
doi:10.1351/PAC-CON-11-03-06
© 2011 IUPAC, Publication date (Web): 7 July 2011

Reprogrammable magnonic crystals formed by interacting ferromagnetic nanowires*

Jesco Topp[1], Georg Duerr[2], Klaus Thurner[2], and Dirk Grundler[2,‡]

[1]Institut für Angewandte Physik und Mikrostrukturforschungszentrum, Universität Hamburg, Junigusstrasse 11, D-20355 Hamburg, Germany; [2]Lehrstuhl für Physik funktionaler Schichtsysteme, Physik Department E10, Technische Universität München, James-Franck-Strasse 1, D-85747 Garching b. München, Germany

Abstract: Spin-wave (SW) modes are addressed which are confined in thin individual $Ni_{80}Fe_{20}$ nanowires with widths ranging from 220 to 360 nm. In periodic arrays with an edge-to-edge separation of down to 100 nm, confined modes of neighboring nanowires are found to couple coherently and form allowed minibands and forbidden frequency gaps. This gives rise to a one-dimensional magnonic crystal. We present all-electrical SW spectroscopy data and micromagnetic simulations. We find that the nanowire arrays allow us to reprogram the relevant magnonic band structure via the magnetic history. A forbidden frequency gap of up to about 1 GHz is controlled by an in-plane magnetic field being as small as a few mT.

Keywords: ferromagnets; ferromagnetic resonance; magnetic properties; magnonics; magnonic crystals; micromagnetic; nanodevices; nanostructured materials; nanowires; spin waves; thin films; transition metals.

INTRODUCTION

Collective spin excitations in ferromagnets have regained great interest. Recent observations such as spin-wave (SW) quantization [1] (cf. Figs. 1a–d), localization [2], and interference [3] have stimulated the field of magnonics where SWs (magnons) are explored in order to carry and process information [4]. Here, novel devices and applications are discussed such as magnonic crystals, i.e., the magnetic counterpart of photonic crystals and SW buses in integrated circuits [5,6]. The dynamic response of individual nanomagnets was controlled in that different magnetic configurations were realized via the magnetic history [7]. It was then shown that confined modes in separate nanomagnets (Figs. 1c,d) couple if the edge-to-edge separation is on the deep-submicron scale. Starting from quantized SW modes in individual nanomagnets, dynamic stray-field interaction then leads to allowed minibands (Figs. 1e,f) [8]. Periodically patterned ferromagnets are thus found to form magnonic crystals [6,9,10]. The minibands allow one to transmit an SW across the chain of nanomagnets, which are separated from each other via an air gap. Here we discuss how such minibands depend on the geometry and magnetic state of the nanomagnets [11]. Varying the width of neighboring wires alters characteristically the field dependence of SW eigenfrequencies and the band structure. Parallel or antiparallel alignment of the neighboring wires' magnetization M is shown to change the allowed minibands and forbidden frequency gaps. Periodically patterned magnetic devices thus open intriguing perspectives for the manipulation of SWs at the nanoscale and the realization of reprogrammable magnetic metamaterials [12].

---

*Paper based on a presentation made at the International Conference on Nanomaterials and Nanotechnology (NANO-2010), Tiruchengode, India, 13–16 December 2010. Other presentations are published in this issue, pp. xxxx–xxxx.

‡Corresponding author: E-mail: grundler@ph.tum.de

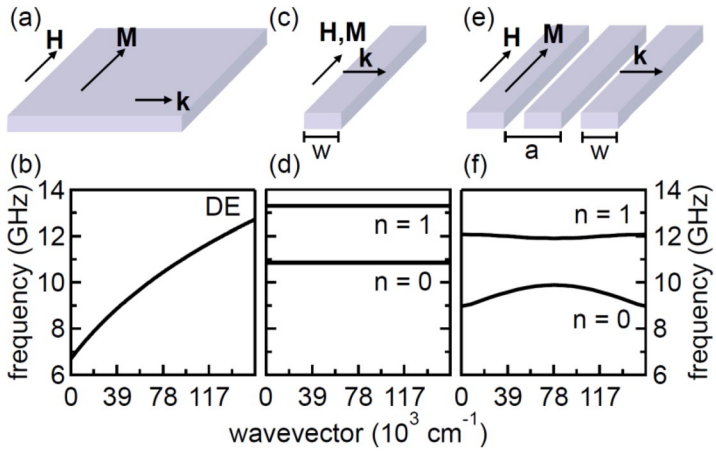

Fig. 1 (a) Relative orientation of magnetization M and wavevector k for a Damon–Eshbach (DE) mode. (b) Dispersion relation, i.e., frequency f vs. wavevector k, for the DE mode. Here we assume a 20-nm-thick permalloy film subject to $\mu_0 H = 50$ mT as indicated. (c) A ferromagnetic wire of width w magnetized along the long axis. (d) Discrete eigenfrequencies are found as a function of wavevector transferred in transverse direction. The quantization is due to confinement by the geometrical edges. From bottom to top, the number n of nodal lines along the wire increases. The eigenfrequencies have been calculated following ref. [14]. (e) Relevant parameters for an array of collinear wires. (f) Dispersion relations of a nanowire array for a wavevector in transverse direction as sketched in (e). Due to dipolar interaction allowed minibands form. We assume here permalloy with a thickness of 20 nm, $w = 300$ nm, and $a = 400$ nm following the theory of ref. [15]. The dynamic interaction and the resulting miniband bandwidth decrease with increasing number n of nodal lines. Note that the dispersions shown in (b), (d), and (f) depend on the effective field inside the ferromagnet and are shifted to higher frequencies with increasing field.

EXPERIMENTAL TECHNIQUES AND SIMULATIONS

Fabrication of ferromagnetic nanowires

Arrays of nanowires were prepared from thermally evaporated Permalloy ($Ni_{80}Fe_{20}$, Py), which had a thickness d between 20 and 26 nm depending on the individual array. We used semi-insulating GaAs as the dielectric substrate. Ferromagnetic resonance (FMR) measurements on unpatterned films yielded a saturation magnetization close to the literature value of $\mu_0 M_{sat} = 1.08$ T. Following ref. [13], the phenomenological damping constant was determined from the power-absorption linewidth as $\alpha = 0.006 \pm 0.001$.

Based on a polymethyl methacrylate (PMMA) 50 K/950 K double-layer resist mask we performed electron-beam lithography and a lift-off process to generate 100- to 180-µm-long Py nanowires which exhibited a width w between 220 and 360 nm. The aspect ratio l/w was greater than 100 for all samples (l is the length). The width w and periodicity a were varied from array to array, i.e., the edge-to-edge separation (a-w) was different. The arrays consisted of up to several hundred nanowires. Previous experiments on nanowires of similar lateral width showed that such wires did not exhibit measurable dipolar interaction at an edge-to-edge separation of about 700 nm and above [16]. We used an in-plane magnetic field H under different orientations to vary the magnetic state of the nanowires. In the following, we assume the wires to be positioned in the (x, y) plane, with the long axis pointing in the y direction. The magnetization M will be decomposed in x, y, and z (out-of-the plane) dynamical components m' when analyzing the mode profiles. We will focus our discussion about experimental data on five arrays #1 to #5. Arrays #1 to #4 consist of nanowires with a large edge-to-edge separation making dipolar coupling effects small. This is different from array #5 where (a-w) is as small as 100 nm. Array #6 consisting of alternating-width wires is considered in micromagnetic simulation only.

Integrated coplanar wave guides

Coplanar waveguides (CPWs) were used to guide microwave magnetic fields to the ferromagnets (Fig. 2a). The CPWs consisted of ground(G)-signal(S)-ground(G) lines. These were prepared on top of the nanowire arrays using lift-off processing of a 150-nm-thick trilayer of Cr, Ag, and Au. SiO_2 layers of 10–50 nm thickness were used as insulating intermediate layers. The CPWs' central conductors had a width w_{CPW} = 10 μm (Fig. 2) or smaller. We used both CPWs with and without optimization with respect to an impedance of Z_0 = 50 Ohm.

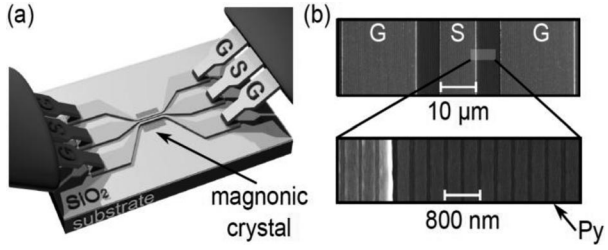

Fig. 2 (a) Sketch of the experiment showing microwave probes in contact with a coplanar waveguide (CPW) consisting of ground (G) and signal (S) lines. The nanowire array (magnonic crystal) is placed in the central part of the CPW. (b) Scanning electron microscopy image of a CPW's central part (upper panel) and nanowires near the edge of the signal line (bottom panel). We show here sample #5.

Broadband SW spectroscopy

The detection of SW excitations was accomplished by broadband microwave absorption measurements. For all-electrical SW spectroscopy, we used a vector network analyzer (VNA) to measure the microwave transmission T through the CPW as a function of the microwave frequency f [17,18]. CPW and VNA were connected through coaxial cables and microwave probes. In Fig. 2, we show a sample where the CPW has been positioned in parallel with the nanowires. Here, both the in-plane and out-of-plane components of the CPW's radio frequency (rf) field h_{rf} were orthogonal with respect to the magnetization M when M was collinear with the easy axis, i.e., the long axis. This means we optimized the torque $M \times h_{rf}$ to induce spin precession through the microwave field. This yielded a large signal-to-noise ratio (SNR). Further samples were prepared where the wires where orthogonal to the CPW. In this case, the signal was considerably weaker at H = 0. For SW spectroscopy in the linear regime a microwave with a small amplitude of $\mu_0 h_{rf}$ = 0.1 mT was chosen to avoid unintentional nonlinear effects [19,20]. When the frequency of a microwave current generated by the VNA matched the resonance frequency f of an SW, a drop in the CPW's transmission occurred due to the resonant absorption of power by the precessing magnetization. We recorded spectra $T(f)$ at different in-plane magnetic fields H using a microwave probe station incorporating two crossed field-coil pairs [21]. Each spectrum was normalized by a reference spectrum, e.g., recorded at $\mu_0 H$ = 90 mT applied along the nanowire's easy axis. At such a high field, SW resonances were at frequencies well above 10 GHz and therefore outside the region of interest. The resulting spectrum $\Delta T(f)$ reflected the dynamic magnetic susceptibility $\chi(f)$ of the nanowires and, in particular, resonances due to SW excitation.

© 2011, IUPAC

Micromagnetic simulations

We use the OOMMF micromagnetic code and apply the one-dimensional periodic-boundary-condition extension [22,23] to model arrays of densely packed magnetic nanowire, which we assume to be infinitively long (Fig. 3). The simulated segment has a volume of 300 × 100 × 19.5 nm³. The OOMMF discretization uses a cell of 5 × 25 × 6.5 nm³. The material parameters are $\mu_0 M_{sat}$ = 1.08 T (saturation magnetization), $A = 13 \times 10^{-12}$ J/m (exchange constant), and γ = 176 GHz/T (gyromagnetic ratio).

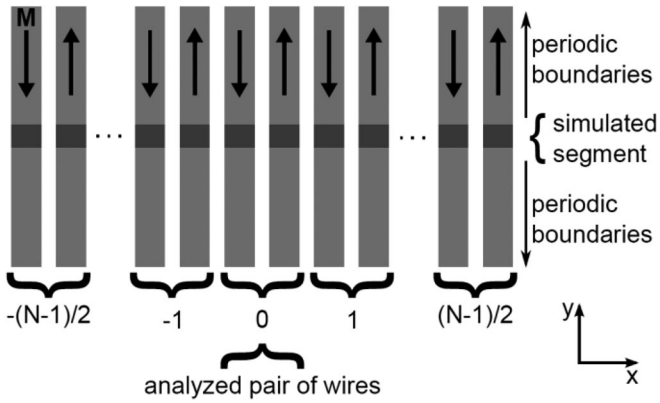

Fig. 3 Sketch of the array of interacting nanowires which we simulate. We consider the small segment as highlighted in dark gray and apply periodic boundary conditions along the wires' long axes. For the mode analysis we evaluate the dynamic magnetization of the central pair of wires labeled "0". We indicate the magnetization M with a bold arrow. Here the wire array is assumed to be in the AFO state where neighboring wires are of opposite magnetization direction. N is the number of wire pairs considered in the simulation. In this work a number larger than N = 9 does not change the dynamics inside the central pair "0".

Due to the infinite length of the nanowires, demagnetization effects in y direction are not relevant. This allows us to choose the simulation cell as a cuboid. In the thin and narrow wires considered here, the remanent magnetization aligns itself with the long axis, being the easy axis due to the large aspect ratio. Starting from quasistatic configurations, we perform dynamic simulations to numerically calculate the eigenmode spectrum. For this, a field pulse h_{rf} of amplitude 1 mT and temporal full-width-half-maximum value of 6 ps is applied. We vary the orientation of h_{rf} to consider different excitation symmetries. We observe changes in the total oscillator strength of modes that will be discussed later, but not in the mode profiles.

To remodel the long-wavelength limit h_{rf} is homogeneous. The spatially resolved discrete Fourier transform of the dynamical component $m'_z(x,y)$ is then analyzed. We average the data and thereby obtain the resonance frequencies of eigenmodes. Simulations on non-interacting nanowires with a relatively large edge-to-edge separation are simulated using the MicroMagus code [24].

SPIN WAVES IN INTERACTING AND NON-INTERACTING NANOWIRES

Spectroscopy and magnetic anisotropy explored in a perpendicular field

We have measured the SW resonance of wires with different w and large edge-to-edge separation, i.e., the separation was beyond 500 nm to minimize dipolar coupling. This was done to explore the magnetic anisotropy (shape anisotropy) of non-interacting wires induced by the nanopatterning. In Fig. 4, eigenfrequencies are shown for three different widths w (arrays #1, #2, and #3). Here we consider the most pronounced mode of largest intensity (n = 0) and apply the in-plane field in a direction perpendi-

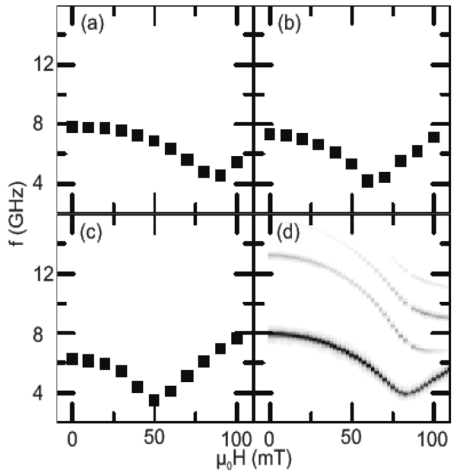

Fig. 4 Experimental data obtained on Py nanowires of different width w which amounts to (a) 220, (b) 280, and (c) 360 nm (arrays #1, #2, and #3, respectively). The mode with $n = 0$ is displayed. The edge-to-edge separation between individual wires was several 100 nm such that, intentionally, dipolar coupling played a minor role or was vanishingly small. The length (thickness) was 100 μm (26 nm). The field H is applied along the x-axis direction. (d) Simulation performed for an array of 280-nm-wide wires with large edge-to-edge separation. The field H was applied at 89.5° with respect to the wires' long axes. Black (gray) indicates large (weak) intensity.

cular to the long axis, i.e., in x-axis direction. The eigenfrequency at $H = 0$ is found to depend characteristically on w. It decreases with increasing width. For increasing field H, the eigenfrequencies of all wires first drop and then rise again. This reflects the well-known hard-axis behavior of an anisotropic micromagnet [25]. The frequency minimum is attributed to an anisotropy field. This field stabilizes the magnetization M along the long axis, i.e., the easy axis. Such wires have two stable remanent configurations at $H = 0$ in that M points either in $+y$ or $-y$ direction depending on the magnetic history. As expected, the anisotropy field decreases with increasing w, i.e., decreasing aspect ratio l/w. In the limit of a plain film and magnetically isotropic Py the anisotropy field should be zero.

The mode shown in Figs. 4a–c is the so-called center mode with $n = 0$, which exhibits the maximum spin-precession amplitude right in the center of the wire [26]. At the edges, the amplitude is reduced due to dipolar pinning. Simulations, which we will discuss later, show a value of about 20 % at the edge for $H = 0$ if compared to the central amplitude (compare also Fig. 2 in ref. [14]). The field dependence of the center mode frequency is well remodeled by the micromagnetic simulations (Fig. 4d). The black symbols exhibit the characteristic behavior observed in the experiments. The simulations show that further higher-order modes can be excited. However, the intensity is much weaker. In the experiments of Figs. 4a–c, the density of the non-interacting wires was small. At the same time, the CPW was perpendicular to the wires' long axes. This reduced the SNR to such a value that we observed the center mode only. Experiments on dense arrays of nanowires showed higher-order modes which resided at higher frequencies than the center mode with $n = 0$ [14,27,28].

Arrays of bistable nanomagnets in a parallel field

In the following we discuss experiments in a magnetic field applied along the y direction. In Figs. 5a,b, spectra are shown for non-interacting 310-nm-wide wires taken in a major and minor loop measurement, respectively. The edge-to-edge separation amounts to 700 nm (array #4). Coming from large positive fields we observe around –15 mT the reversal of the wires' magnetization. Due to the switching field distribution the intensities at the two relevant eigenfrequencies change gradually between –13 and

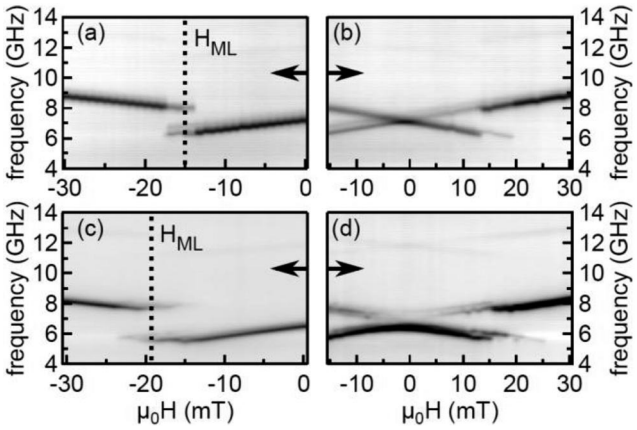

Fig. 5 Spectra (gray-scale plot) obtained on an array of non-interacting 310-nm-wide wires having an edge-to-edge separation of 700 nm (array #4): (a) major loop data taken after saturation at +90 mT and (b) minor loop (ML) data obtained after applying +90 and –15 mT. For such data a crossing of branches is observed close to $H = 0$. Dark color stands for large power absorption. Spectra taken for an array of interacting 300-nm-wide wires with an edge-to-edge separation of 100-nm (array #5): (c) major loop data taken after saturation at +90 mT and (d) ML data obtained after applying +90 and –19 mT. Here an avoided crossing behavior is observed. Near 12 GHz higher-order modes of weak intensity are found. The magnetic field is always collinear with the long axis. Arrows indicate the sweep directions of the magnetic field. The vertical broken line highlights the field position where the intensities suggest the reversal of about 50 % of the wires. Here the ML measurements started. For clarity, we depict data in (b) and (d) for the same field regime.

–18 mT in Fig. 5a. Below –18 mT the bistable nanowires are reversed to the opposite direction if compared to the initial state at large positive fields.

In the minor loop (ML) measurement of Fig. 5b we start from –15 mT and increase the field H. There are two pronounced branches of almost the same intensity, which have a different slope as a function of H. They cross close to $H = 0$, giving rise to a maximum in intensity at $f = 7$ GHz. This behavior is attributed to an array of wires where about 50 % of the wires have been magnetized in $-y$ direction at –15 mT and 50 % have remained magnetized in $+y$ direction. For $\mu_0 H > 20$ mT, all nanowires are aligned with the magnetic field pointing in $+y$ direction, and a single branch with maximum intensity is found.

For 300-nm-wide nanowires with an edge-to-edge separation of only 100 nm (array #5), the major loop measurement shown in Fig. 5c provides similar data if compared to Fig. 5a. Here the reversal of wires occurs around –19 mT. The ML data of Fig. 5d where we have taken spectra starting at $\mu_0 H =$ –19 mT show, however, a novel behavior if compared to (b). Now the branch of lowest frequency is of almost maximum intensity for a wide field regime between –15 and +15 mT. In addition, this branch does not really cross with a higher-frequency branch of opposite slope. Instead, we find an avoided crossing behavior around $H = 0$. The anticrossing mode at higher frequency is of very weak intensity. We have recently shown that the avoided crossing behavior is characteristic for a magnonic crystal which is formed by dipolarly coupled nanowires and where neighboring wires are magnetized in opposite directions. This is the so-called antiferromagnetic order (AFO) state [11]. The relevant magnonic band structure will be discussed later. Before that it is instructive to consider micromagnetic simulations and spatial profiles of the precession amplitudes in neighboring wires.

© 2011, IUPAC

Simulated precession profiles of confined modes coherently coupled between nanowires

Nanowires of identical width

In Fig. 6 we show simulation data obtained on 300-nm-wide wires exhibiting an edge-to-edge separation of 100 nm (array #5). We assume $N = 9$. A larger N does not alter the dynamics of the central wires substantially. In (a) and (b) we consider two different orientations of the rf magnetic field h_{rf}. In (a) h_{rf} is collinear with the x direction, i.e., the hard-axis direction. We show simulations for the AFO state. The comparison with Fig. 5d provides a very good agreement concerning the field dependence, avoided crossing behavior and relative intensities. A discrepancy remains with the absolute frequencies. This can be explained by a reduced dipolar interaction in the real array if compared with the ideal array in the simulations. This can be attributed to variations in the periodicity a and width w due to unintentional roughness [11]. If h_{rf} is pointing along the z (out-of-plane) direction the relative intensities of the modes are changed. This reflects that some of the modes exhibit symmetric and some antisymmetric mode profiles as will be discussed below. Convincingly, the eigenfrequencies are the same in Figs. 6a,b. In (b) branches of relatively large intensity are found between 12 and 14 GHz originating from higher-order modes. These are found to be weak in (a) and, correspondingly, in the experimental data of Fig. 5d.

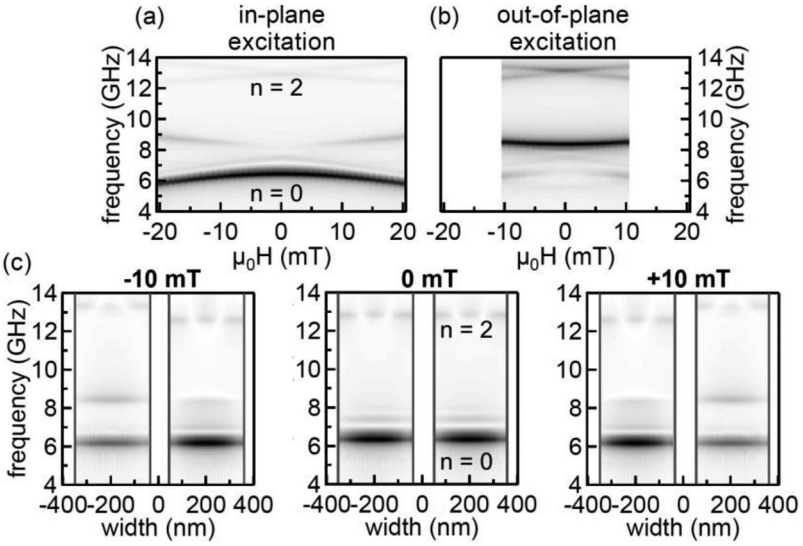

Fig. 6 Micromagnetic simulations of array #5: the spectra in (a) and (b) are obtained for two different orientations of the rf magnetic field h_{rf} as indicated on the top. (c) Spin precession profiles as a function of the x coordinate in the wires. We consider three different fields H applied along the y direction. Black indicates large spin precession amplitude. The graphs in c have been obtained for excitation with an in-plane field h_{rf}.

We now analyze the mode profiles of the central pair of nanowires as defined in Fig. 3. We first present intensities as gray-scale plots in Figs. 6 and 7. Then relative phases will be discussed below. We consider two wires in the unit cell of the periodic lattice, which are magnetized in an antiparallel configuration, i.e., the AFO state. In Fig. 6c, h_{rf} is assumed to be parallel to the hard axis. The low-frequency branch at $H = 0$ is an excitation where both wires exhibit precession profiles similar to a center mode. Here, the number n of nodal lines inside a single wire is zero. Changing $\mu_0 H$ to +10 and –10 mT, we observe that the spin precession in the two wires stay at a common frequency. It decreases slightly with both positive and negative H. The behavior of the lowest eigenfrequency $n = 0$ is thus peculiar. The center modes are coherently coupled in the wires of antiparallel magnetization M. This is different from

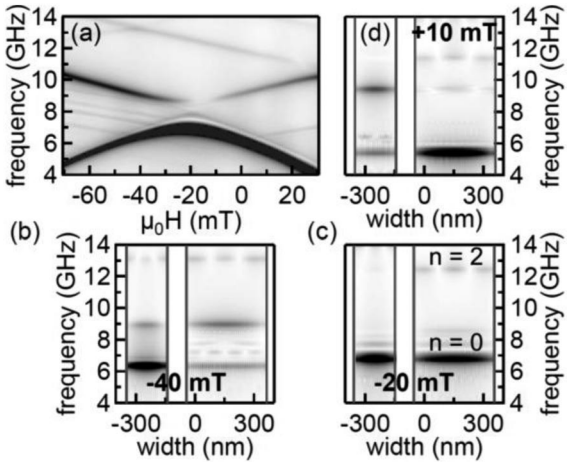

Fig. 7 Micromagnetic simulations for array #6 exhibiting a unit cell with two wires of widths w_1 = 200 nm and w_2 = 400 nm. The edge separation is 100 nm. (a) Field dependence of the SW eigenfrequencies. The graphs in (b), (c), and (d) show spin precession profiles (intensity) in x direction for three different fields H applied in y direction. Black indicates large spin precession intensity.

non-interacting nanowires and reflects the interaction via dynamic dipolar coupling through rf stray fields [11]. Interestingly, the relative intensities change between the wires of the unit cell when H is at positive or negative values. This is consistent with an avoided crossing behavior. Modes with $n > 0$ residing at higher frequencies do not seem to couple coherently in the unit cell over a broad field regime. Between 12 and 14 GHz modes exist which exhibit two nodal lines (n = 2). At $\mu_0|H|$ = 10 mT one finds a frequency difference of about 1 GHz between the n = 2 modes of the individual wires of the unit cell. Due to the involved precession profile the dynamic stray field between the wires is reduced if compared to n = 0. This leads to a smaller interaction and coupling strength.

Periodic array of alternating-width nanowires

The characteristic features discussed above, i.e., a common frequency of the low-frequency mode and shifting of relative intensities between modes of neighboring wires, are also found in an array where neighboring wires exhibit a different width. In Figs. 7a–d we depict a set of simulation results for wires with widths w_1 = 200 nm and w_2 = 400 nm (array #6). The edge-to-edge separation is 100 nm. Due to the different widths w_1 and w_2 the confinement effect is expected to be different. Studying the arrays #1, #2, and #3 we have shown that the eigenfrequency of confined modes in nanowires depend characteristically on the geometrical width (Fig. 4). Based on this, we would expect the eigenfrequencies of wires with w_1 and w_2 to differ by at least 2 GHz at H = 0. This is not the case in Fig. 7. Instead, the simulations in Figs. 7b,c,d show that the center modes with n = 0 precess at the same eigenfrequency of about 6 GHz. The common eigenfrequency shifts with H. For the array of alternating-width wires the center modes show the maximum precession amplitudes simultaneously in both wires of the unit cell when a field of –20 mT is applied. If H deviates from this field value the relative intensities vary in a way which is consistent with the avoided crossing. The center modes are thus coherently coupled over a broad field regime. Higher-order modes do not show such a broad coupling regime. Near $\mu_0 H$ = –40 mT, modes with n = 2 seem to precess coherently coupled.

REPROGRAMMABLE MAGNONIC CRYSTALS FORMED BY INTERACTING NANOWIRES

Band structure considerations

In this section, we discuss the magnon dispersions $f(k)$ for an array of identical wires for different remanent states. We revisit band structures which have been reported in ref. [11] and were found to depend on the magnetic history. The formalism provides information about the phase differences existing between the precessing spins in neighboring wires. In Figs. 8a,b, we show dispersions for the ferromagnetic-order (FMO) and AFO state, respectively, calculated at $H = 0$ by the approach reported in ref. [15]. The calculated band structures are found to be different for the two states. In (b) the number of allowed minibands is doubled with respect to (a). This is because the unit cell of the periodic lattice is larger and consists of two nanowires being magnetized in opposite directions. For $n = 0$, one finds an acoustic and an optical branch in Fig. 8b. At the lowest frequency the components m'_x of neighboring wires precess in phase at $k = 0$ (acoustic mode). The next higher-lying eigenfrequency belongs to the optical mode where the components m'_x of neighboring wires precess out-of-phase at $k = 0$. The relative phase is consistent with the mode $n = 0$ of Fig. 8a when considered at the original boundary of the first Brillouin zone (BZ) ($k = 78 \times 10^3$ cm^{-1}). Figures 8a,b show that the nanowires of array #5 form a magnonic crystal where the band structure is reprogrammed via the magnetic history [11]. In the AFO state the relevant widths of the allowed minibands are below 1 GHz and only about half the value if compared to the FMO state.

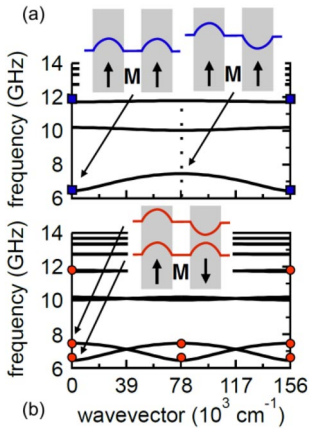

Fig. 8 Band structure for array #5 calculated following ref. [15] at $H = 0$ when (a) all nanowires are magnetized in parallel and (b) neighboring nanowires exhibit antiparallel M. The insets show schematically the amplitudes and relative phases of the dynamical in-plane components m'_x for selected eigenfrequencies and wavevectors k. The dotted line in (a) at 78×10^3 cm^{-1} marks the BZ boundary given by the periodicity $a = 400$ nm of array #5. In (b) the BZ boundary is at 39×10^3 cm^{-1}. The symbols are data points measured at $k \approx 0$.

Recently, Brillouin light scattering was used to investigate such features experimentally as a function of wavevector k in nanowire arrays of different geometrical parameters [29]. The data showed the reprogrammable band structures for arrays consisting of alternating-width nanowires. The avoided crossing behavior observed for the acoustic and optical magnon modes in Figs. 5d and 6a is a characteristic feature of a magnonic crystal and can be used to identify the underlying AFO state in a spatially averaging spectroscopy experiment. Microscopic details of the avoided crossings will be discussed in detail elsewhere [30].

© 2011, IUPAC

Operational characteristics of a reprogrammable magnonic crystal

Magnonic crystals such as the one shown in Fig. 8 (array #5) offer the control of SW propagation at the nanoscale. To illustrate this, we consider an SW with a wavelength $\lambda = 4a$ (Fig. 9). The corresponding wavevector k amounts to $k = 2\pi/\lambda = 2\pi/4a = \pi/2a$. This value corresponds to the BZ boundary $k_{BZ,AFO}$ of the magnonic crystal in the AFO state. Such an SW can propagate through the magnonic crystal in both the FMO and AFO state at $H = 0$ (Figs. 9a,b, respectively). If a small in-plane magnetic field is applied in the AFO state, the scenario changes. A forbidden frequency gap Δ opens at $k = \pi/2a$ (Fig. 9c). An SW with $k = \pi/2a$ and an eigenfrequency residing in the gap Δ is expected to stop. The different band structure and propagation characteristics can be attributed to the different effective (internal) field H_{eff} of the nanowires in the FMO and AFO state. Consider a small in-plane magnetic field as sketched in Fig. 10. In (a), i.e., the FMO state, each wire of array #5 experiences the same field value H_{eff}. The SW with $\lambda = 4a$ can propagate along the periodic chain of nanowires.

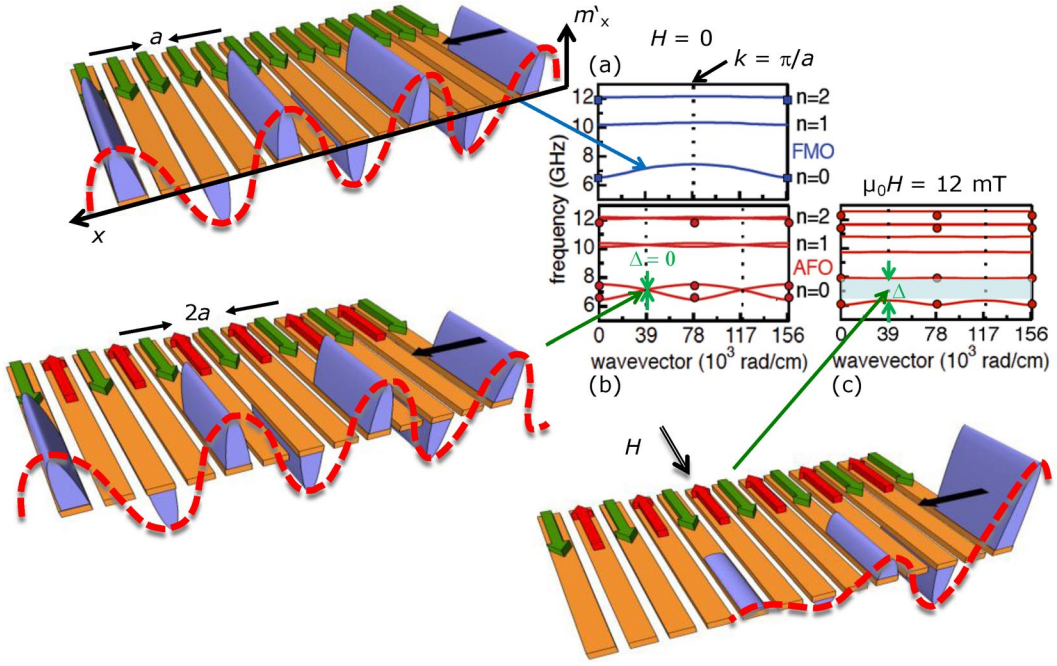

Fig. 9 Illustration of SW propagation through array #5 for three different experimental scenarios: (a) FMO state at $H = 0$, (b) AFO state at $H = 0$, and (c) AFO state with an in-plane field $H <> 0$. The relevant band structures for $H = 0$ and $\mu_0 H = 12$ mT are taken from ref. [11]. The vertical dotted lines indicate BZ boundaries; symbols reflect experimental data. We consider an SW propagating in x direction (as indicated by the arrow) and having a wave length of $\lambda = 4a$. We show a schematic snapshot of the in-plane precession amplitudes m'_x when there is a node in every second nanowire. The broken line highlights the plane-wave character of the coupled spin excitation. The bold arrows indicate the directions of the nanowires' magnetization M.

The scenario is different when the same field is applied to the AFO state. Depending on the direction of M the effective field is either positive or negative in each of the wires in Fig. 10b. Since the orientation of M is alternating with a period of $2a$ the effective field obeys the same periodicity. If now viewed as a periodic potential of non-zero amplitude a spin wave with $\lambda = 4a$, i.e., $k = \pi/2a = k_{BZ,AFO}$ is expected to experience coherent backscattering (Bragg reflection) giving rise to a forbidden frequency gap. An SW with an eigenfrequency in the gap becomes an evanescent mode which is expo-

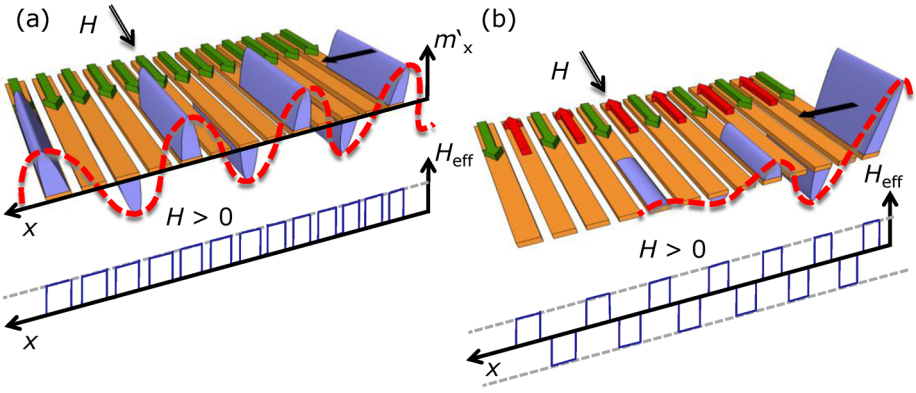

Fig. 10 The spatial variation of the effective field H_{eff} is different for the (a) FMO and (b) AFO state if one applies an in-plane field H as indicated. In (a) the value of H_{eff} is constant from wire to wire. In (b) the field H_{eff} changes sign in the unit cell consisting of two wires and exhibits a periodicity of $2a$.

nentially damped inside the magnonic crystal. For an applied field of 12 mT, the forbidden frequency gap is found to be about 1.3 GHz at the BZ boundary in Fig. 9. At the same time, the widths of the allowed minibands decrease.

The different states FMO and AFO, which are generated by a different magnetic history, thus allow us to control the functionality of the magnonic crystal. This goes beyond photonic or plasmonic crystals. Since SWs in the GHz frequency regime have a wavelength λ which is orders of magnitude shorter than electromagnetic waves at the same frequency magnonic crystals offer microwave devices such as filters and logic gates operated on the nanoscale.

CONCLUSIONS

We have investigated SW resonances in narrow ferromagnetic nanowires from $Ni_{80}Fe_{20}$, both experimentally and theoretically. Arrays consisting of about 300-nm-wide nanowires show magnonic crystal behavior for an edge-to-edge separation of 100 nm. Using all-electrical broadband SW spectroscopy and micromagnetic simulations we have studied in detail the modes which are relevant for the formation of the allowed minibands. We have addressed both arrays of identical wires and alternating-width wires. Both form magnonic crystals where the SW band structure is in particular "reprogrammed" via the magnetic history. For the lowest-order mode the interaction-induced miniband is found to have a width of about 1 GHz or below depending on the magnetic ordering of the array. In case of identical nanowires an in-plane magnetic field of a few mT is found to create a forbidden frequency gap at the BZ boundary when neighboring wires are magnetized in an antiparallel configuration. Nanoscale microwave devices with field-controlled reflection and transmission might be envisioned.

ACKNOWLEDGMENTS

We gratefully acknowledge collaborations and discussions with G. Gubbiotti, D. Heitmann, M. Kostylev, V. Kruglyak, and S. Neusser. The research leading to these results has received funding from the European Community's Seventh Framework Programme (FP7/2007-2013) under Grant Agreement No. 228673, from SFB 668, Nanospintronics of the City of Hamburg, and the German Excellence Cluster "Nanosystems Initiative Munich".

© 2011, IUPAC

REFERENCES

1. J. Jorzick, S. O. Demokritov, C. Mathieu, B. Hillebrands, B. Bartenlian, C. Chappert, F. Rousseaux, A. N. Slavin. *Phys. Rev. B* **60**, 15194 (1999).
2. J. Jorzick, S. O. Demokritov, B. Hillebrands, M. Bailleul, C. Fermon, K. Y. Guslienko, A. N. Slavin, D. V. Berkov, N. L. Gorn. *Phys. Rev. Lett*. **88**, 047204 (2002).
3. J. Podbielski, F. Giesen, D. Grundler. *Phys. Rev. Lett.* **96**, 167207 (2006).
4. S. Neusser, D. Grundler. *Adv. Mater.* **21**, 2927 (2009).
5. A. Khitun, M. Bao, K. L. Wang. *J. Phys. D: Appl. Phys.* **43**, 264005 (2010).
6. V. V. Kruglyak, S. O. Demokritov, D. Grundler. *J. Phys. D: Appl. Phys.* **43**, 264001 (2010).
7. F. Giesen, J. Podbielski, T. Korn, M. Steiner, A. van Staa, D. Grundler. *Appl. Phys. Lett.* **86**, 112510 (2005).
8. (a) G. Gubbiotti, S. Tacchi, G. Carlotti, N. Singh, S. Goolaup, A. O. Adeyeye, M. Kostylev. *Appl. Phys. Lett.* **90**, 092503 (2007); (b) M. Kostylev, P. Schrader, R. L. Stamps, G. Gubbiotti, G. Carlotti, A. O. Adeyeye, S. Goolaup, N. Singh. *Appl. Phys. Lett.* **92**, 132504 (2008); (c) M. P. Kostylev, A. A. Stashkevich. *Phys. Rev. B* **81**, 054418 (2010).
9. Z. K. Wang, V. L. Zhang, H. S. Lim, S. C. Ng, M. H. Kuok, S. Jain, A. O. Adeyeye. *Appl. Phys. Lett.* **94**, 083112 (2009).
10. G. Gubbiotti, S. Tacchi, M. Madami, G. Carlotti, A. O. Adeyeye, M. Kostylev. *J. Phys. D: Appl. Phys.* **43**, 264003 (2010).
11. J. Topp, D. Heitmann, M. P. Kostylev, D. Grundler. *Phys. Rev. Lett*. **104**, 207205 (2010).
12. V. V. Kruglyak, P. S. Keatley, A. Neudert, R. J. Hicken, J. R. Childress, J. A. Katine. *Phys. Rev. Lett.* **104**, 027201 (2010).
13. S. Kalarickal, P. Krivosik, M. Wu, C. E. Patton. *J. Appl. Phys.* **99**, 093909 (2006).
14. K. Yu. Guslienko, S. O. Demokritov, B. Hillebrands, A. N. Slavin. *Phys. Rev. B* **66**, 132402 (2002).
15. M. P. Kostylev, A. A. Stashkevich, N. A. Sergeeva. *Phys. Rev. B* **69**, 064408 (2004).
16. J. Topp, J. Podbielski, D. Heitmann, D. Grundler. *Phys. Rev. B* **78**, 024431 (2008).
17. J. Podbielski, F. Giesen, M. Berginski, N. Hoyer, D. Grundler. *Superlattices Microstruct.* **37**, 341 (2005).
18. S. Neusser, G. Duerr, H. G. Bauer, S. Tacchi, M. Madami, G. Woltersdorf, G. Gubbiotti, C. H. Back, D. Grundler. *Phys. Rev. Lett.* **105**, 067208 (2010).
19. J. Podbielski, D. Heitmann, D. Grundler. *Phys. Rev. Lett.* **99**, 207202 (2007).
20. J. Topp, D. Heitmann, D. Grundler. *Phys. Rev. B* **80**, 174421 (2009).
21. F. Giesen, J. Podbielski, T. Korn, D. Grundler. *J. Appl. Phys.* **97**, 10A712 (2005).
22. M. Donahue, D. G. Porter. *National Institute of Standards and Technology Interagency Report NISTIR* **6376**, <http://math.nist.gov/oommf/> (1999).
23. K. M. Lebecki, M. J. Donahue, M. W. Gutowski. *J. Phys. D* **41**, 175005 (2008).
24. D. V. Berkov, N. L. Gorn. Micromagus, software for micromagnetic simulations, <www.micromagus.de> (2008).
25. (a) J. Lindner, K. Baberschke. *J. Phys.: Condens. Matter* **15**, R193 (2003); (b) Y. Roussigné, S. M. Chérif, P. Moch. *J. Magn. Magn. Mater.* **268**, 89 (2004); (c) R. D. McMichael, B. B. Maranville. *Phys. Rev. B* **74**, 024424 (2006).
26. (a) J. P. Park, P. Eames, D. M. Engebretson, J. Berezovsky, P. A. Crowell. *Phys. Rev. Lett.* **89**, 277201 (2002); (b) C. Bayer, J. P. Park, H. Wang, M. Yan, C. E. Campbell, P. A. Crowell. *Phys. Rev. B* **69**, 134401 (2004).
27. J. Topp, J. Podbielski, D. Heitmann, D. Grundler. *J. Appl. Phys.* **105**, 07D302 (2009).
28. M. Bailleul, D. Olligs, C. Fermon. *Phys. Rev. Lett.* **91**, 137204 (2003).

© 2011, IUPAC

29. S. Tacchi, M. Madami, G. Gubbiotti, G. Carlotti, S. Goolaup, A .O. Adeyeye, N. Singh, M. P. Kostylev. *Phys. Rev. B* **82**, 184408 (2010).
30. J. Topp, S. Mendach, D. Heitmann, M. P. Kostylev, D. Grundler. Unpublished.

© 2011, IUPAC